Renewable and Sustainable Energy Reviews 112 (2019) 158–169

Contents lists available at ScienceDirect

Renewable and Sustainable Energy Reviews

journal homepage: www.elsevier.com/locate/rser

Strategies for engineering phonon transport in Heusler thermoelectric compounds

Sadeq Hooshmand Zaferani[a,c,*], Reza Ghomashchi[a,b,**], Daryoosh Vashaee[c,d,***]

[a] School of Mechanical Engineering, University of Adelaide, SA, 5005, Australia
[b] ARC Research Hub for Graphene Enabled Industry Transformation, University of Adelaide, Adelaide, SA, 5005, Australia
[c] Department of Electrical and Computer Engineering, North Carolina State University, NC, 27606, United States
[d] Department of Materials Science and Engineering, North Carolina State University, NC, 27606, United States

ARTICLE INFO

Keywords:
Thermoelectricity
Heusler alloys
Thermal conductivity
Phonon scattering
Waste heat recovery

ABSTRACT

Thermoelectric generators, which can convert waste heat directly into electricity, are promising candidates for capturing low-grade heat and enhancing the efficiency of the heat engines. This would lead to decreasing the fossil fuel usage and greenhouse gas emission. Many Heusler compounds have been studied for thermoelectric application due to their desired characteristics such as sizeable thermoelectric power factor, non-toxicity, and high stability over a wide temperature range. The primary restriction for Heusler thermoelectric materials has been their high lattice thermal conductivity, which reduces their thermoelectric figure of merit. Several strategies have been carried out to ameliorate this restriction by engineering the phonon transport properties. This article discusses several approaches such as bulk nanostructuring, the creation of point defects and vacancies, impurity doping, and multiphase engineering of the material structure for reducing the thermal conductivity of the Heusler compounds. The effectiveness of each of these methods depends on temperature; hence, the working temperature must be taken into account when designing the material structure and the composition to achieve the optimum performance for practical applications.

1. Introduction

Climate change as a result of global warming may be traced back to human activities, industrial processes, and greenhouse gas emission [1,2]. In this field, the application of renewable energy and the practical use of waste heat are very appealing fields of study [3–6]. Apparently, the trend is encouraging as based on the report of "international energy agency, world energy outlook 2017", there has been a rapid deployment of clean energy technologies and an indirect falling costs [7]. One of the available techniques towards improving energy efficiency is to endeavor to convert the wasted thermal energy back into more useful energy such as electricity. Thermoelectric generators (TEGs), capable of converting waste heat directly into electricity, have already attracted worldwide attention as evidenced by the expansion of research activities on thermoelectric materials and manufacturing of TE modules and systems. Waste heat recovery is an environmentally friendly method which not only reduces the consumption of fossil fuels for energy production but also decreases waste heat emissions [8–11].

For thermoelectric materials, the dimensionless figure of merit (zT) is a measure for evaluating the efficiency of energy conversion and is defined as:

$$zT = \frac{S^2\sigma}{\kappa_e + \kappa_l}T \tag{1}$$

where S is the Seebeck coefficient (VK^{-1}), σ is the electrical conductivity ($\Omega^{-1}m^{-1}$), T is temperature (K), κ_e and κ_l are the electronic and the lattice thermal conductivities ($Wm^{-1}K^{-1}$), respectively [12,13]. With the advances in new thermoelectric materials, the thermoelectric technology is growing to find new market space for power generation, cooling, or detection and imaging applications [14–17]. Consequently, new types of thermoelectric devices and fabrication techniques are also being developed [18,19]. High-performance thermoelectric materials have been promoted following new designs such as the reduction of the thermal conductivity by using larger phonon

* Corresponding author. School of Mechanical Engineering, University of Adelaide, SA, 5005, Australia.
** Corresponding author. School of Mechanical Engineering, University of Adelaide, SA, 5005, Australia.
*** Corresponding author. Department of Electrical and Computer Engineering, North Carolina State University, NC, 27606, United States.
E-mail addresses: sadeq.hooshmandzaferani@adelaide.edu.au (S. Hooshmand Zaferani), reza.ghomashchi@adelaie.edu.au (R. Ghomashchi), d.vashaee@ncsu.edu (D. Vashaee).

https://doi.org/10.1016/j.rser.2019.05.051
Received 23 September 2018; Received in revised form 3 May 2019; Accepted 22 May 2019
Available online 30 May 2019
1364-0321/

scattering via nanostructuring [20,21] and nano-inclusions [22–24] as well as the increase of the power factor by designing complex structures [25–29], creating of resonant energy levels close to the band edges [30], using low dimensional structures [31–33], and via carrier filtering [34–36]. New materials based on bulk heterostructures, or nano-composites, have especially taken considerations because of their simplicity of manufacture and similarity with the current type of the thermoelectric devices. Even though nanostructuring techniques have turned out to be gainful in numerous material frameworks because of the inherent spectral discrepancies of the electron and phonon transport parameters [37], these strategies are also linked to the degradation of the charge carrier mobility or have less efficiency at high working temperatures. Therefore, in a few materials, they have resulted in a significant decrease in the power factor prompting little or no enhancement of the figure-of-merit [20,38,39].

In this regard, Heusler alloys have a simple lattice structure and as such phonon characteristics compared to those of the caged structures like Skutterudites [40–42] and Clathrates [43–45]. Therefore, they generally have higher thermal conductivity while also a more substantial thermoelectric power factor. Therefore, methods for reducing the thermal conduction in Heusler based alloys are highly desired. Concerning material selection, it is desired to find compounds containing nontoxic and eco-friendly elements with no or little rare earth components, which are sustainable in harsh condition and at high temperature In this field, the Heusler compounds have attracted much attention due to their particular characteristics as non-toxic materials with magnetic or semiconducting behavior and also remarkable stability at various temperature intervals [46,47].

These compounds are divided into full- and half-Heusler types which are based on ternary intermetallic materials [48–53] with the stoichiometric composition of X_2YZ and XYZ, respectively [12,54]. The full-Heusler alloys (X_2YZ) have an $L2_1$ structure with fcc lattice unit cells containing four atoms as X at (1/4,1/4,1/4) and (3/4,3/4,3/4), Y at (1/2,1/2,1/2) and Z at (0,0,0) in Wyckoff coordinates, and their corresponding space group is Fm-3m (No. 225) [12,54]. Also, the half-Heusler alloys have a C1b structure with the absence of one of the X sub-lattices, and the corresponding space group of F-43 m (No. 216) [12,54].

In the mentioned compositions, generally, X is filled with a high valence transition element, Y is substituted with a lower valence transition metal atom, and finally, Z is an element in the III–V columns of the periodic table with s-p type valence electrons [12,54].

Fig. 1 shows the atomic arrangements for the full-Heusler and half-Heusler alloys and the elements, which have been carried out in these compounds.

Traditionally, high thermal conductivity ($\kappa = \kappa_e + \kappa_l$) has been the main drawback of the Heusler TE alloys. The dominant part of this thermal conductivity is κ_l due to lattice vibration which is represented by phonons [58,59]. Generally, phonons are described in quantum mechanics as a unit of vibrational energy that arises from oscillating atoms within a crystal lattice, which can have different frequencies, and are responsible for transferring the thermal energy. There are two types of phonons to carry thermal energy within solids, (i) acoustic phonons which are representing the coherent displacement of atoms in parallel (longitudinal) or perpendicular (transverse) to the propagation and (ii) optical phonons, corresponding to the incoherent motion of the two neighboring atoms in the opposite direction.

Fig. 2.b shows the schematic optical and acoustic components of phonon energies based on the dispersion of two atoms with masses of m_1 and m_2 (equation (2)) [60].

$$\omega^2 = \beta\left(\frac{1}{m_1} + \frac{1}{m_2}\right) \pm \sqrt{\left(\frac{1}{m_1} + \frac{1}{m_2}\right)^2 - \frac{4sin^2qa}{m_1 m_2}} \tag{2}$$

Here ω is the frequency, a the lattice constant, q the phonon wave vector, and β a constant related to the atomic bonds.

As depicted in Fig. 2.a, in the acoustic branches, including longitudinal (LA) and transverse (TA) modes, the group velocities of all the acoustic branches, $V_{gj} = d\omega_j/dq$ (j = LA, TA), are higher than that of the longitudinal optical (LO) and transverse optical (TO) modes with their velocity being nearly zero at $q \approx 0$. The transverse mode makes either a doubly degenerate or two separate branches. In each classification, the transverse modes have lower group velocity than the longitudinal ones due to the higher frequency of the longitudinal modes at a specific wave vector. In other words, the longitudinal branches generally carry more energies in comparison to the transverse branches with the same momentum.

In a solid, if A represents the number of atoms in a unit cell, the outcome will be 3A phonon branches, in which, three branches are acoustic, and the rest are optical. Also, Table 1 shows the classification of acoustic and optical branches as longitudinal and transverse with their counts [61].

Moreover, both the acoustic and optical components of phonon energy propagate transversally and longitudinally within the crystalline solids as schematically illustrated in Fig. 2.b. In respect to the application temperature range, the transverse acoustic (TA) (Fig. 2b) branches have low frequency and are characteristics of low temperature while the longitudinal acoustic (LA) (Fig. 2b) types have higher frequencies and are dominant at high temperature.

It is worth noting that a higher number of atoms (A) in a unit cell can be a recipe for obtaining lower thermal conductivity. Because, when the number of optical components of the phonon energy increases, the absorbed energy can be transferred less by the acoustic branches. In this case, more energy is attributed to the optical branches, which have a negligible contribution to heat transfer ascribed to their low group velocity. Moreover, due to the limited phonon frequency (~10 THz), by increasing the optical branches, the acoustic phonon frequency declines as the acoustic branches transfer only a partial amount of energy in the crystal. This fact influences the lattice thermal conductivity mostly at high temperature in which the high-frequency phonons are the majority of heat carriers [61].

To reduce thermal conductivity, one needs to somehow obstruct the phonon transport [62,63] with appropriate strategies. The choice of phonon scattering approach is based on the application temperature range, which may include strategies such as nanostructuring [62–66], impurity/vacancy doping [67] and designing a multiphase matrix [12]. Consequently, a comprehensive understanding of the phonon scattering mechanisms is required for optimum engineering of the material structure. The following section discusses the central phonon scattering mechanisms useful for the Heusler TEs.

2. Thermal conductivity of heusler compounds

The lattice thermal conductivity in the isotropic Debye approximation can be described based on Holland's model [68]:

$$\kappa = \frac{1}{3}\left(2I_{T_0} + 2I_{T_U} + I_L\right) \tag{3}$$

where

$$I_j = \frac{k_B}{2\pi^2 v_{gj}}\left(\frac{k_B}{\hbar}\right)^3 \int_{x_{j_2}}^{x_{j_1}} \tau_{cj} \frac{x^4 e^x}{(e^x - 1)^2} dx \tag{4}$$

Here $x = \hbar\omega/k_B T$ is a dimensionless parameter, k_B is the Boltzmann constant, h is the Plank's constant ($\hbar = h/2\pi$), θ_j and v_{gj} are the Debye temperature and the group velocity for the corresponding phonon modes, respectively, T states the absolute temperature, ω is the phonon frequency, and τ_{cj} shows the total scattering relaxation time for the corresponding phonon branch.

Parameters j, x_{j_1}, x_{j_2}, and x_{j_3} are defined in Table 2.

ω_1 corresponds to $q_{max}/2$ where the transverse branch becomes almost flat (Fig. 2a). This is the frequency where umklapp processes are

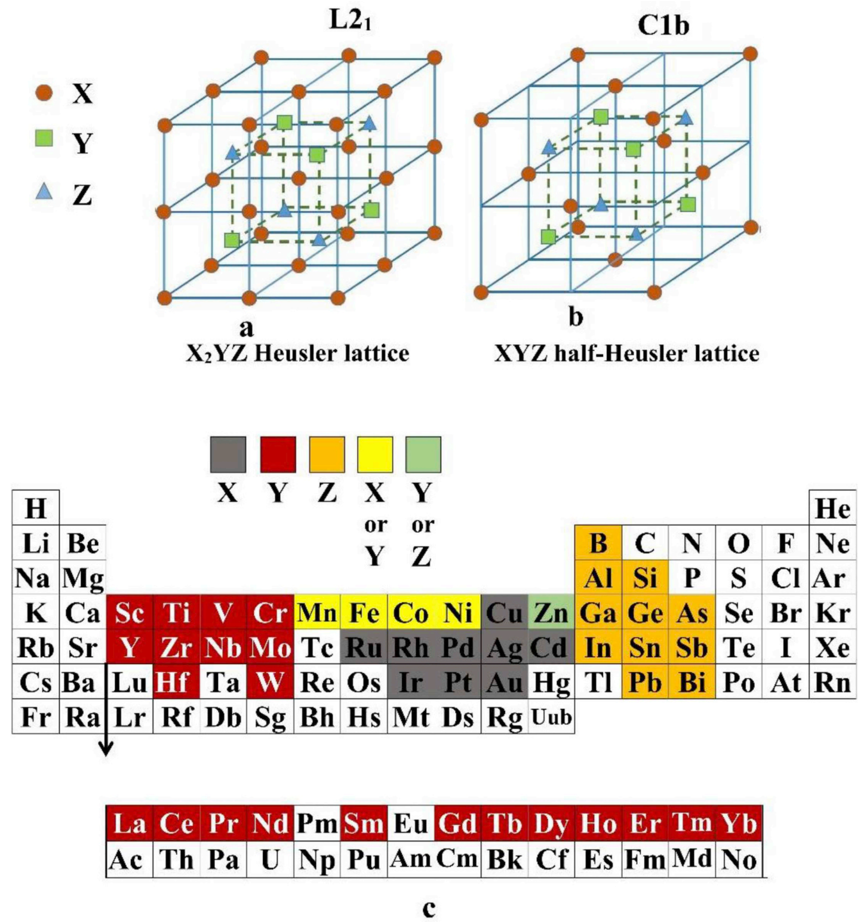

Fig. 1. (a) full-Heusler crystal structures and (b) half-Heusler, (c) specific elements in the Heusler alloys (adapted from Refs. [55–57]).

supposed to start. ω_2 and ω_3 are the zone-boundary frequencies for the transverse and longitudinal phonons, respectively.

This model reduces to the Callaway's model [69,70] if the longitudinal phonons dominate the thermal conduction. Callaway's formalism makes no distinction between transverse and longitudinal phonon modes and the sum over phonon polarization is set equal to three, and an average phonon velocity is used everywhere. Therefore, the Callaway model becomes less accurate when the temperature increases. Holland's model, also, although not being as accurate as the first principle methods, enables obtaining detailed information about the effect of different phonon scattering mechanisms on lattice thermal conductivity in a convenient way. There are several main contributing scattering sources within solid structures incorporated in the phonon scattering relaxation time. Table 3 lists the summary of the main phonon scattering mechanisms and the corresponding relaxation times including, grain boundary phonon scattering, impurity-phonon mass fluctuation scattering, point defect (alloy) scattering, three-phonon scattering due to the normal (N) and umklapp (U) processes, and electron-phonon scattering.

Table 1
The number of acoustic and optical branches in a solid with A atom in the unit cell.

	Longitudinal	Transverse
Acoustic	1	2
Optical	A-1	2(A-1)

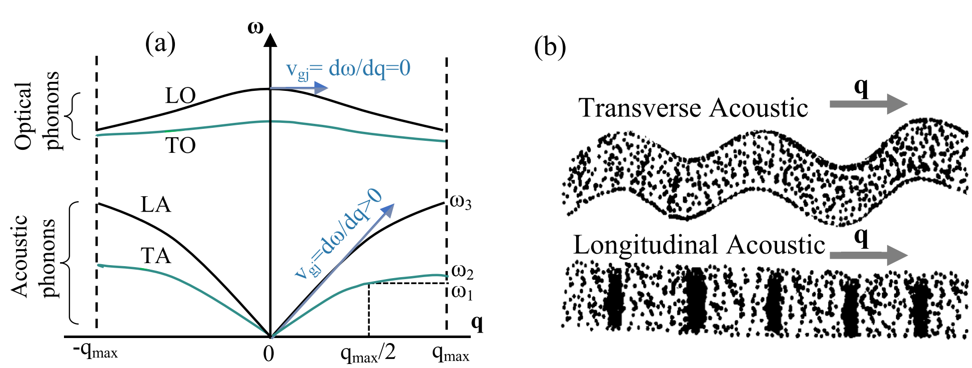

Fig. 2. Schematic acoustic and optical phonon branches for a diatomic lattice.

Table 2
Parameters used in equations (3) and (4).

Parameters	Values		
j	T_0	T_U	L
x_{j1}	0	$\hbar\omega_1/k_B$	0
x_{j2}	$\hbar\omega_1/k_B$	$\hbar\omega_2/k_B$	$\hbar\omega_3/k_B$

Here M is the total average mass for the alloy, γ is the Grüneisen constant (or the anharmonicity parameter), a is the atomic size determined by the cubic root of the atomic volume, and β is the ratio of the normal three phonon-scattering rate to the umklapp three-phonon-scattering rate, which is assumed temperature-independent. Electron-phonon relaxation timeτ_{e-ph}, is given by Ziman [74,75] in which ν_s is the sound velocity, k_B is the Boltzmann constant, E_a is the deformation potential, m_d is the density-of-states effective mass, ρ is the mass density, and E_F is the Fermi energy. y_i, M_i, and $a_i$in the relaxation time due to point defects are the fractional concentration, mass, and atomic size of each element in the alloy respectively, where $M = \sum_i f_i M_i$and $a = \sum_i f_i a_i$. ε_s determines the contribution of strain disorder to point defect scattering of phonons. If the lattice constants of the elements in the compound do not differ largely, the effect of strain is small compared with the mass fluctuation. The phonon relaxation time due to scattering by impurity atoms is calculated based on a single atomic site, in which f_i is the fractional concentration of the impurity atom i, and M_i is its mass. Due to the substitutional replacement of the host atoms by impurities, the doping-phonon scattering in Heusler alloys can happen via both the mass fluctuating and atomic interaction. Therefore, it follows a similar trend as that of the point defects.

Grain boundaries can introduce three different types of scattering of phonons: (1) regular reflection and refractionτ_{Ref},(2) diffusive scattering due to the corrugation of the GB, τ_{Diff}, and (3) Rayleigh scattering, τ_{Ray} [76,77]. Diffusive scattering is related to the physical defects at the GB, such as vacancy. Rayleigh scattering arises from the mass and bond stiffness differences between the host alloy and the spherical grains such as precipitated regions of impurities. The mean free path due to regular reflection and refraction is approximately constant as listed in the table. Here $\ell_{GB}$is the mean distance of the GBs, and $\Delta\nu$ is the difference of refraction indices of the elastic waves in different grains. This can arise, for example, due to the different orientation of the crystal in the adjacent grains. If the crystal orientation is slightly rotated by an angle δ, one can estimate $\Delta\nu \approx \delta$. If the GB region is much smaller than the wavelengths of the excited phonons, the diffusive scattering relaxation time changes with ω^{-2}. The phonon relaxation time with respect to such a diffusive scattering is shown in Table 3, in which η is a parameter that characterizes the degree of the corrugation of the GB (typically $1 < \eta < 10$). For the case of Rayleigh scattering, in which Ξ is some constant dependent on the details of the grain boundary characteristics, the approximation is valid for low frequency phonons. At high frequencies the exponent of ω decreases and eventually at very high frequencies, the scattering is almost frequency-independent and is in the same form as that of the regular reflections and refractions at the GBs [76,77].

Once all the different relaxation times are calculated, the total relaxation time of phonons τ_c can be given by Matthiessen's rule [78] as follows:

$$\frac{1}{\tau_c} = \frac{1}{\tau_U} + \frac{1}{\tau_N} + \frac{1}{\tau_{e-ph}} + \frac{1}{\tau_{pd}} + \frac{1}{\tau_{i-ph}} + \frac{1}{\tau_{Ref}} + \frac{1}{\tau_{Diff}} + \frac{1}{\tau_{Ray}} \tag{5}$$

However, the strength and effectiveness of each scattering mechanism is temperature dependent. At low temperature and low frequency, grain boundary phonon scattering is often ruling, and at a sufficiently high temperature and high phonon frequency, the Umklapp scattering of phonon by other phonons becomes dominant. At the intermediate temperature and frequency (between the two limits) electron-phonon and point defect scattering, e.g., by dopants, vacancies, and alloy element substitution can become important (Fig. 3). Therefore, the working temperature must be considered when engineering the structure for optimum performance from the scattering resources.

3. Scattering mechanisms

To reduce the thermal conductivity of Heusler TE alloys, one may engineer various sources of the phonon scattering such as grain boundaries or inter-phase boundaries (interface), interstitial or substitutional atoms, impurities, point defects (e.g., substitutional, vacancies) and precipitates [48]. Over approximately the last ten years, many of these techniques have been successfully implemented. Table 4 shows a range of Heusler compounds synthesized and the executed phonon scattering mechanisms within the working temperature range. The success of producing appropriate sample is dependent on the process parameters such as time, temperature, dopant and the degree of porosity. As represented in this table, the mass fluctuating is a practical method of phonon scattering, which has been employed in various alloys such as $Yb_{13.82}Pr_{0.18}Mn_{1.01}Sb_{10.99}$ $La_{2.2}Ca_{0.78}Te_4$ and $Ti_{0.5}Zr_{0.5}NiSn_{0.994}Sb_{0.006}$ leading to zT values of 1.2, 1.2 and 1, respectively.

Table 3
Phonon scattering relaxation time [71–73].

Scattering Strategies	Parameters and relations
GB regular reflection and refraction	$\tau_{Ref} \sim \ell_{GB} v_{gj}^{-1} (\Delta\nu)^{-2}$
GB diffusive scattering	$\tau_{Diff} \sim \ell_{GB} v_{gj}^{-1} \left(\frac{k_B \theta_j}{\hbar\omega}\right)^2 \frac{1}{\eta}$
GB Rayleigh scattering	$\tau_{Ray} \sim \left(\frac{v_{gj}}{\ell_{GB}}\right)^3 \left(\frac{\theta_j}{T\omega}\right)^4 \Xi$
Impurity-phonon mass fluctuation	$\frac{1}{\tau_{i-ph}} = \left(\frac{a}{v_{gj}}\right)^3 \left(\frac{k_B T}{\hbar}\right)^4 \sum_i f_i \left(1 - \frac{M_i}{M}\right)^2 x^4$
Point defect	$\frac{1}{\tau_{PD}} = \left(\frac{a}{v_{gj}}\right)^3 \left(\frac{k_B T}{\hbar}\right)^4 \sum_i \left[y_i \left(1 - \frac{M_i}{M}\right)^2 + \varepsilon_s y_i \left(1 - \frac{a_i}{a}\right)^2\right] x^4$
3-phonon Umklapp process	$\tau_u^{-1} = \frac{20\pi}{3} \hbar N_A \left(\frac{6\pi^2}{4}\right)^{1/3} \times \frac{1 + \frac{5}{9}\beta}{1 + \beta} \frac{\gamma^2}{Ma^2} \left(\frac{T}{\theta_j}\right)^3 x^2$
Normal three-phonon scattering	$\tau_N = \beta \tau_u$
Electron-phonon	$\tau_{e-ph}^{-1} = E_a^2 m_d^3 v_{gj} / 4\pi\hbar^4 \rho \left(\frac{1}{2} m_d v_{gj}^2 / k_B T\right) \times \ln\left(\frac{1 + \exp\left(-\left(\frac{1}{2} m_d v_{gj}^2 / k_B T\right) + E_F / k_B T - x^2 / 16\left(\frac{1}{2} m_d v_{gj}^2 / k_B T\right) + x/2\right)}{1 + \exp\left(-\left(\frac{1}{2} m_d v_{gj}^2 / k_B T\right) + E_F / k_B T - x^2 / 16\left(\frac{1}{2} m_d v_{gj}^2 / k_B T\right) - x/2\right)}\right)$

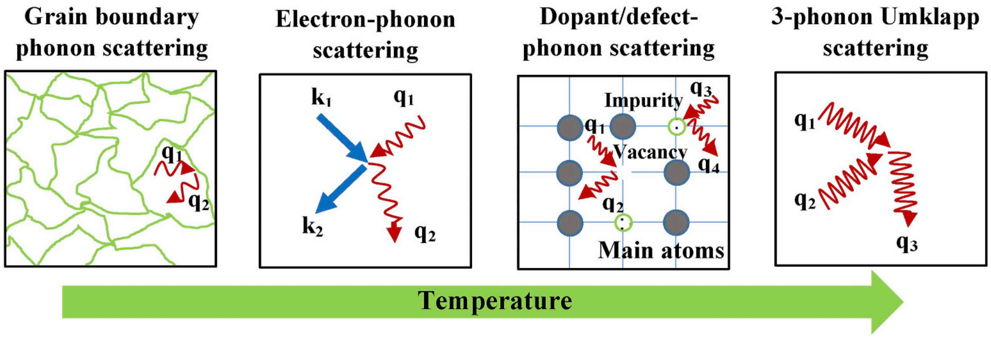

Fig. 3. Dominant modes of the phonon scattering versus temperature (adapted from Ref. [61]).

3.1. Grain boundaries scattering

Grain boundaries as phonon scatterers can be employed in designing the TE materials. The correlation between phonon coherencies and the mean free path, the wavelength, and grain size (characterized length) have impacts on phonon dispersion. Thermal conductivity decreases when the effective phonon mean free path is greater than the grain or crystal size [94]. Since phonon mean free path is a function on the wavelength, and wavelength itself is dependent on temperature as per Wien's displacement law ($\lambda_{max}.T$ = constant), grain boundaries can be the significant scattering sources at low temperature [92,93].

For the Heusler TE alloys, nano-sized grains [47,63,64] and high-density of grain boundaries have resulted in phonon scattering and reduced the lattice thermal conductivity. For example, the reported lattice thermal conductivity of the polycrystalline $Zr_{0.5}Hf_{0.5}Co_{1-x}Rh_xSb_{0.99}Sn_{0.01}$ was 3.7 $Wm^{-1}K^{-1}$ at 300 K in structures with grain sizes of 80-175 nm. Mikami et al. [95] used spark plasma sintering to synthesize $Fe_2VAl_{0.9}Si_{0.1}$/Bi composites via incorporating different amounts of Bi to yield a composite structure containing micrometer-sized Bi grains and nanometer-sized Fe_2VAl grains. The results showed the inclusion of nanometer-sized microstructural constituents of $Fe_2VAl_{0.9}Si_{0.1}$ has reduced thermal conductivity [95].

Also, Katsuyama et al. [96] studied the effects of grain refining via the milling process on the thermal conductivity of half-Heusler $ZrNiSn_{0.98}Sb_{0.02}$ alloys. Fig. 4 illustrates the grain size reduction of this alloy with increasing the milling time.

Table 5 compares the TE properties of different samples. As represented in the table, the thermal conductivity lowers with the milling time in the 3 and 5-h milled samples due to the grain refinement, hence; a higher concentration of the grain boundaries.

It is noted that the sample milled for three hours has higher Seebeck coefficient than the one milled for five hours resulting in a higher zT. The grain refinement can lead to the formation of various defects such as vacancies, antisites, dislocations, etc., some of which can introduce charge carriers into the lattice [97–99]. The lower Seebeck coefficient and higher electrical conductivity of the 5-h milled sample indicates a higher carrier concentration, which can be the reason for the smaller power factor if the carrier concentration is away from the optimum value [97,100]. There is also a limit for the grain size below which the carrier mobility is impaired more than the phonon transport, which can lead to smaller zT [97,100].

In another study [101], the relation between the average grain size and the lattice thermal conductivity was evaluated for $TiNiSn_{1-x}Sb_x$ alloy as shown in Fig. 5.

In this study, the lattice thermal conductivities were characterized against the average grain size in the temperature range up to 300 K. As shown in Fig. 5, by decreasing the average grain diameters, the lattice thermal conductivity decreased due to the interface phonon scattering. It should be noted that the grain boundaries can also act as potential obstacles to hinder the charge carrier transport and decrease electrical conductivity [47]. In some materials, the effect is significant, that the zT does not improve noticeably or even reduces [102,103].

Therefore, the decoupling of thermal and electrical conductivities is desired. El-Asfoury et al. [104] used graphene to decouple the κ and σ

Table 4
List of Heusler TE compounds with dominant scattering sources and the corresponding temperature range.

Heusler TE Compound	Engineering Strategy	Effective Temperature Range (K)	Scattering Mechanism	ZT Max	Ref.
ZrNiSn	Y or Sb doping	–	Mass fluctuating	0.28	[58]
$\mathbf{Ti_{0.3}(ZrHf)_{0.69}V_{0.01}Ni_{0.9}Pd_{0.1}Sn_{0.99}Sb_{0.01}}$	Ti substitution at the Zr and Hf site	820	Mass fluctuating	0.92	[79]
$\mathbf{Ti_{0.5}(ZrHf)_{0.49}Nb_{0.01}Ni_{0.9}\ Pd_{0.1}Sn_{0.98}Sb_{0.02}}$	Nb substitution at the IV metal site	900	Mass fluctuating	0.66	[80]
$\mathbf{Mg_2Si_{0.8}Sn_{0.2}}$	Sb doping	740	Mass fluctuating	0.95	[81]
$\mathbf{Zr_{0.5}Hf_{0.5}Co_{0.4}Rh_{0.6}\ Sb_{0.8}Sn_{0.2}}$	Variation of CoSb particle size range	775	Grain boundary scattering	0.18	[82]
$\mathbf{Zr_{0.7}Hf_{0.3}NiSn}$	Phase separation	350	Multi-phase interface scattering	0.007	[83]
$\mathbf{ZrNiSn, (Zr_{0.5}, Hf_{0.5})NiSn}$ $\mathbf{Zr(Ni,Co_{0.2})Sn}$	Ni and/or Co antisites, structural vacancies	775	Mass fluctuating	0.03	[84]
$\mathbf{Ti_{0.3}Zr_{0.35}Hf_{0.35}Ni_{1.01}Sn}$	Phase separation	350–500	Multi-phase interface scattering	0.68	[85]
$\mathbf{Cu_{12}Sb_{3.39}Te_{0.61}S_{13}}$	Te doping	623	Mass fluctuating	0.8	[86]
$\mathbf{AgSbSe_2}$	Sb deficiencies	300–610	Mass fluctuating	1	[87]
$\mathbf{Yb_{13.82}Pr_{0.18}Mn_{1.01}Sb_{10.99}}$	(RE = Pr and Sm) doping	1275	Mass fluctuating	1.2	[88]
CoSbS	Nickel doping	873	Mass fluctuating	0.5	[89]
$\mathbf{La_{2.2}Ca_{0.78}Te_4}$	Calcium doping	1273	Mass fluctuating	1.2	[90]
$\mathbf{Bi_2Te_{2.2}Se_{0.8}}$	Point defecting and Se Content changing	473	Mass fluctuating	0.82	[91]
$\mathbf{Ti_{0.25}Hf_{0.75}CoSb_{0.85}Sn_{0.15}}$	Phase separation	710	Multi-phase interface scattering	1.2	[92]
$\mathbf{Zr_{0.25}Hf_{0.25}Ti_{0.5}NiSn_{0.994}Sb_{0.006}}$	Nano-sized precipitates	500	Mass fluctuating	0.91	[93]
$\mathbf{(Ti_{0.2},Zr_{0.8})Ni_{1.1}Sn}$	FH-nanoprecipitates and Ti, Zr point defects	870	Mass fluctuating	0.81	[65]
$\mathbf{Ru_2VAl_{0.25}Ga_{0.75}}$	Variation of Ga content	400	Mass fluctuating	0.006	[69]
$\mathbf{Ti_{0.5}Zr_{0.5}NiSn_{0.994}Sb_{0.006}}$	HfO_2 doping	500	Mass fluctuating	1	[47]

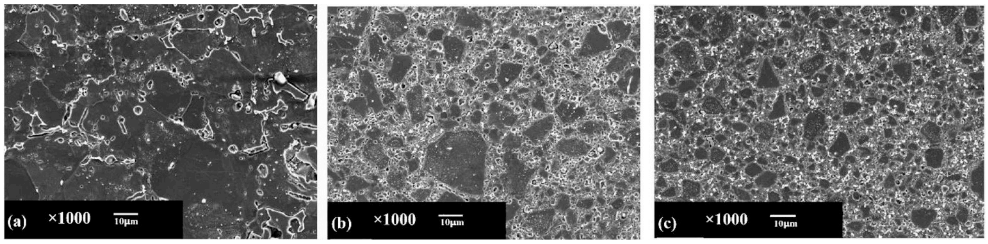

Fig. 4. SEM illustration of grain size reduction due to the milling process in the consolidated samples, a) 0 h, b) 3 h, c) 5 h (ref. [96] with permission).

of the $Bi_{85}Sb_{15}$ compound. In this work, graphene was incorporated in the microstructure to decorate the grain boundaries and prevent crystal growth. Also, the decrease in electrical conductivity was compensated by increasing the carrier concentration (n) via the graphene doping [104–106]. It is also noteworthy that high values of σ/κ and n/κ_l ratios can be regarded as a measure to promote decoupling between thermal and electrical conductivities and arriving at high zT values [104,107].

3.2. Mass fluctuation

Mass fluctuating can also promote the phonon scattering and lower the lattice thermal conductivity [101,108,109]. The magnitude of the mass difference at the interfaces is a crucial parameter in reducing the thermal conductivity [61]. By increasing the temperature, the phonon's wavelength decrease, and these short wavelengths can be scattered more efficiently by mass fluctuation defects such as dislocations, impurities, vacancies and alloy atoms [67].

Also, the change in atomic mass impacts the group velocities. Based on equation (6), by considering the sound speed in solids (V_s) as the group velocity of phonons, via changing the density (ρ) and/or chemical bonding (E), the group velocity will be altered, as well.

$$V_s = \sqrt{\frac{E}{\rho}} \tag{6}$$

Therefore, by selecting the high atomic mass dopant/impurity elements and/or weak chemical bonds, the sound speed will reduce and result in the reduction of thermal conductivity [62,66,67]. This issue can be explained based on the spring-mass system (equation (7)).

$$F = m_i \times a_i = m_i.(d^2X_i/dt^2) = K_i \times X_i \tag{7}$$

In this system, the phonons can be scattered based on the variation in mass (m_i) and/or spring constant (K_i), here representing the atomic bonding. Therefore, atomic substitution/doping is an effective method for modifying phonon transport similar to changing m_i or K_i (Fig. 6).

The change in the mass and/or spring constant occurs due to the presence of impurities or vacancies which can cause mass fluctuation [67]. Moreover, the mass fluctuation can also lead to electric potential disturbance; therefore, it can be employed for energy filtering of both phonons and electrons. This can occur at the interfaces between two different elements or structures. Chai et al. [65] investigated the interfaces between full-Heusler and half Heusler phases to prevent the low energy phonons from passing through the solid structure.

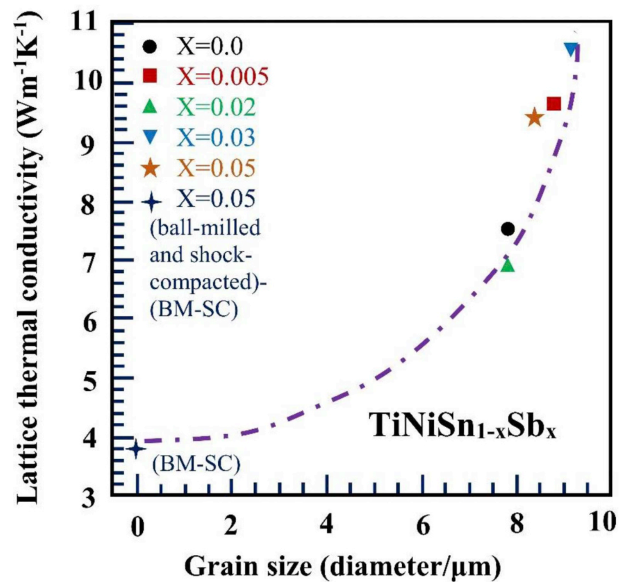

Fig. 5. Relation between the grain size and the lattice thermal conductivity (adapted from Ref. [101]).

In this field, Berry et al. [110] investigated the effects of the mass fluctuating strategy via modulation doping (dissolving) of half-metallic MnNiSb in the TiNiSn alloy and forming a heavily doped $Ti_{1-x}Mn_xNiSn_{1-x}Sb_x$ phase. The results showed the enhancement of the thermoelectric characteristics (Table 6) with a maximum zT value of 0.63 in x = 0.05, at 823 K.

Fig. 7 illustrates BSE images of the modulation doping systems with various amounts of MnNiSb. Based on this image, the matrix was mainly the pristine TiNiSn phase, containing the heavily doped $Ti_{1-x}Mn_xNiSn_{1-x}Sb_x$ with a random distribution. This change in mass caused the fluctuation which led to phonon scattering and reduction of thermal conductivities from about 6.35 to 5.65 $WK^{-1}m^{-1}$at 823 k [110].

Furthermore, nanoinclusions, or nanograins, can provide some barriers to prevent the low energy carriers from propagating through the solid. Hence, both σ and κ will be modified which can generate greater zT values depending on the effectiveness of the barrier on each property [111].

Table 5
Thermoelectric parameters of ZrNiSn alloy after doping with Sb and also refining under the milling process at a temperature of 573 K (adapted from Ref. [96]).

Alloy	S (μVK^{-1})	σ (Scm^{-1})	PF ($\mu Wm^{-1}K^{-2}$)	κ ($Wm^{-1}K^{-1}$)	zT
ZrNiSn	−293	400	3500	7.3	0.25
$ZrNiSn_{0.98}Sb_{0.02}$ 0 h milling	−55	2000	4900	6.7	0.42
$ZrNiSn_{0.98}Sb_{0.02}$ 3 h milling	−180	1724	6700	5.75	0.67
$ZrNiSn_{0.98}Sb_{0.02}$ 5 h milling	−75	1923	5400	5.7	0.55

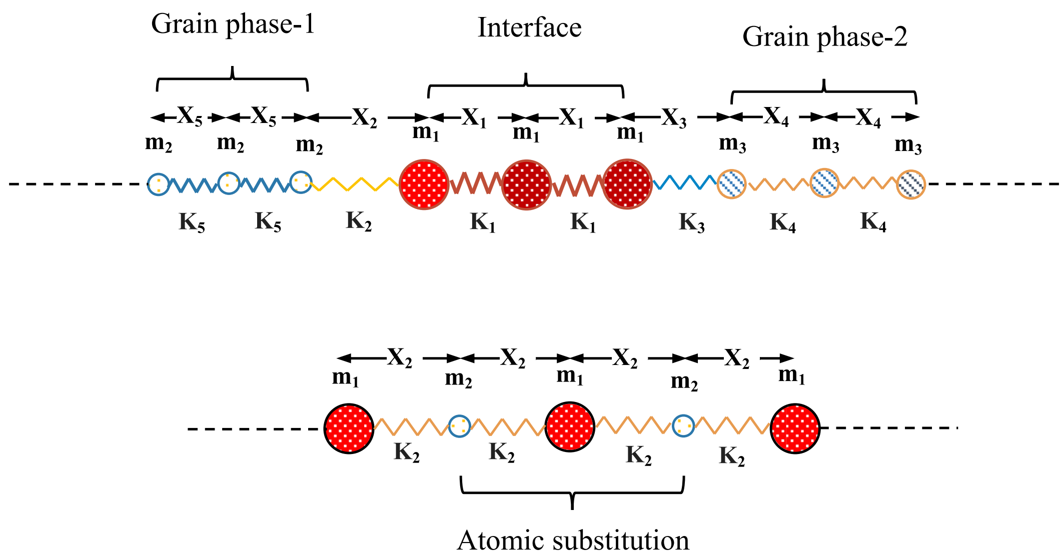

Fig. 6. Motion of atoms in spring system a) using an interface layer with three ranges of atoms, b) atomic substation.

Table 6
Thermoelectric parameters of $(TiNiSn)_{0.95}$ + $(MnNiSb)_{0.05}$ alloy at 823 K [110].

Alloy	S (μVK^{-1})	σ (Scm^{-1})	κ_L ($Wm^{-1}K^{-1}$)	zT
$(TiNiSn)_{0.95}$ + $(MnNiSb)_{0.05}$	−160	1700	3.5@823K	0.63
TiNiSn	−150	1100	4.25 @723K	0.35

In another study, Maji et al. [84] observed the drastic descend of the lattice thermal conductivity in $Zr_{0.5}Hf_{0.5}Co_{1-x}Rh_xSb_{0.99}Sn_{0.01}$ half-Heusler alloy via mass and strain fluctuation by Rh substitution at the Co sites. The effect of Sb doping on thermoelectric characteristics of the full-Heusler Fe_2VAl alloy was evaluated [112]. The results showed that the thermal conductivity remarkably decreased by the Sb substitution of the Al atoms. In this case, the mass fluctuating occurred in the $Fe_2VAl_{1-x}Sb_x$ alloy was due to the large mass difference of Sb and the constituent elements [112]. In another study [79], Zr, Hf, and Ti were utilized to change the mass and strain field caused by their different masses and atomic radii in the $Ti_x(ZrHf)_{0.99-x}V_{0.01}Ni_{0.9}Pd_{0.1}Sn_{0.99}Sb_{0.01}$ half-Heusler alloy. Based on the results, the best thermoelectric properties achieved were $S = -206\ \mu VK^{-1}$, $\sigma = 1408.5\ Scm^{-1}$, $\kappa = 5.13\ W m^{-1} K^{-1}$, and finally, zT = 0.92 at 820 K for x_{Ti} equals to 0.3.

As shown in Fig. 3, vacancies or voids can also provide mass fluctuations. Vacancies can be regarded as weightless nano-sized impurities or point defects which can scatter high-frequency phonons. Lee et al. [80] illustrated the influences of the vacancies on thermal conductivity by increasing the Nb concentration in $Ti_{0.5}(ZrHf)_{0.49}Nb_xNi_{0.9}Pd_{0.1}Sn_{0.98}Sb_{0.02}$, which induced voids in NiSn phase. The sample showed a thermal conductivity reduction from 6.20 to 5 $WK^{-1}m^{-1}$ with the highest zT of 0.66 at 900 k.

The electrical conductivity may be reduced substantially by the addition of the alloying element in the Heusler TEs. The added elements can interact with the Heusler alloy constituent elements either by dissolving (substitutionally or interstitially) in the matrix or forming the second phase precipitates both of which impacting the electrical conductivity [113]. Therefore, the trade-off between the thermal and electrical conductivities must be carefully considered in the mass fluctuation engineering similar to the other scattering strategies, e.g., nanostructuring [25].

3.3. Multi-phases phonon scattering

Another effective technique to scatter phonon is based on the multi-phase engineering of the material structure. Domain interfaces corresponding to multi-phases can generate mass or lattice spacing discontinuity that can scatter phonons, and reduce the lattice thermal conductivity [12,64,114]. In the multi-phase structures, the coexisting Heusler phases (half or full) can be modeled by introducing different K_i and m_i values (equation (7)) corresponding to the different atoms and chemical bonds. The variations in the K_i and m_i lead to scatterings at the phase interfaces affecting the thermal conductivity. At sufficiently large grain sizes, each phase has its own physical properties (and

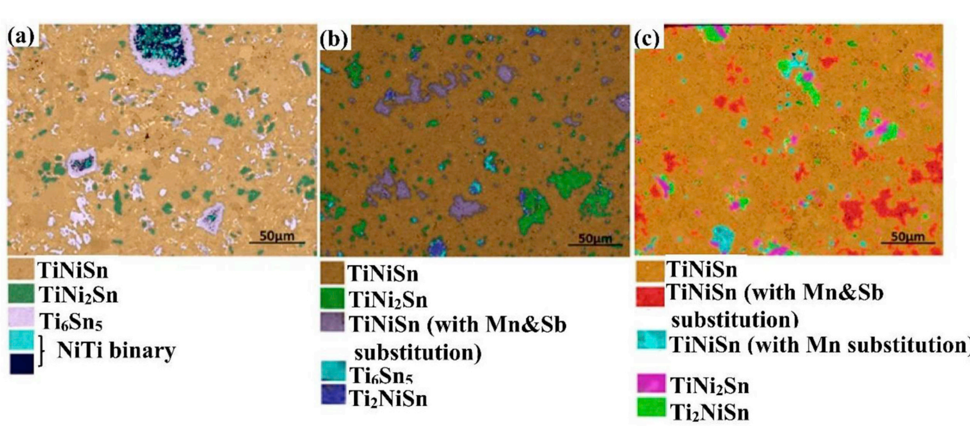

Fig. 7. Backscatter electron (BSE) images of $(TiNiSn)_{1-x}$ + $(MnNiSb)_x$ system: (a) x = 0, (b) x = 0.05, and (c) x = 0.1 (Ref. [110] with permission).

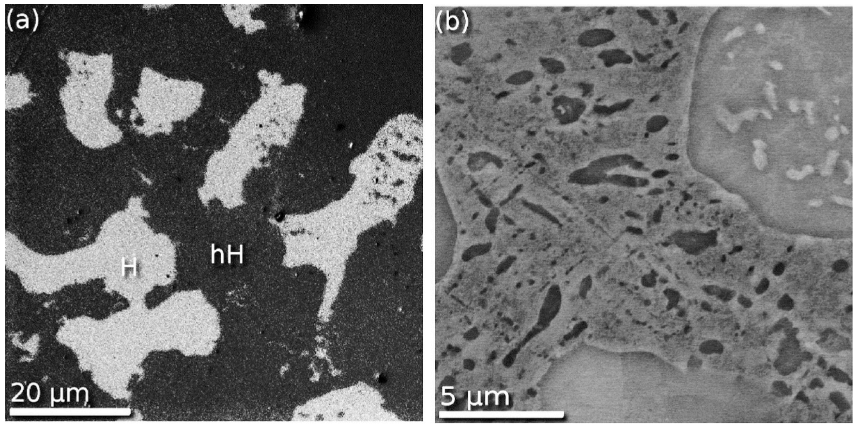

Fig. 8. (a) Optical and (b) scanning electron images of polished surfaces of the binary phase $TiNi_{1.15}Sn$ alloy. In (a), H stands for the $TiNi_2Sn$ full-Heusler alloy, and hH shows the TiNiSn half-Heusler phase (hH). (b) Illustration of a region containing half-Heusler precipitates. (Ref. [118] with permission).

phonon group velocity), and the multi-phase effect can be modeled merely by a phonon scattering causing by the interfaces. However, when the domains become small and comparable to the dominant phonon wavelengths, the individual phase properties alter. In that case, the phonon dispersion (and velocity) changes, and the models based on an effective medium, such as coherent potential approximation, are more appropriate [115–117]. Douglas [118] showed the effects of phase separation on the thermoelectric factors of half-Heusler TiNiSn in corresponding to the presence of phase-segregated Heusler $TiNi_2Sn$ alloy. In this study, the $TiNi_{1.15}Sn$ containing two phases of $TiNi_2Sn$ and TiNiSn (Fig. 8) showed a significant reduction of the thermal conductivity by nearly 10%–30%. Hence, the zT value increased by about 25% compared to that of the TiNiSn alloy reaching 0.44 at 800 K.

Also, as shown in Table 4, the phase separation strategy was carried out successfully to enhance the zT value of the $Ti_{0.25}Hf_{0.75}CoSb_{0.85}Sn_{0.15}$ alloy to around 1.2 at 710 K. In this study, the phase separated half-Heusler $Ti_{0.25}Hf_{0.75}CoSb_{0.85}Sn_{0.15}$ alloy was synthesized, which showed the reduction of thermal conductivities.

Solidification and cooling procedures can influence the phase decomposition because the atomic diffusion is dependent on the cooling rates and temperatures. Consequently, the formation of the new phases can interfere with phonon transport due to differences in phase structure and atomic arrangement [12]. Fig. 9 shows the effects of temperature on phase transformation and segregation of CoVSn compounds within a specific mole percent to the alloy mixture.

According to Table 7, the phase composition can be adjusted by temperature leading to the formation of one to three different phases at each specific molar ratio of the elements in CoVSn (Fig. 9). Each phase has its own thermal and electrical properties; therefore, the composite material can take a wide range of properties depending on the choice of the molar ratios and the temperature of thermal treatment. Thus by controlling the temperature, the multiphase structures could be engineered to introduce the required conditions towards phonon scattering at the phase boundaries.

Schwall et al. [83] evaluated the effects of phase separation on the thermal conductivities of the half-Heusler $Zr_{(1-x)}Hf_xNiSn$ series. They showed that the samples with more phases have higher electrical conductivity, but lower thermal conductivity, despite their higher electronic thermal conductivity. The small thermal conductivity of these samples was associated with the phase separation, which leads to increased interfacial phonon scattering.

Similar to the mass fluctuation mechanism, energy filtering may also occur at the interface of the domains [119]. For example, Agarwal et al. [105] doped graphene into Bi_2Te_3 to make energy filtering that not only decreased the thermal conductivity but also improved the Seebeck coefficient ($S = -117$ ($\mu V.K^{-1}$)). The samples showed $zT = 0.92$ near 405 K. It was concluded that the phase separation induced sub-micron multi-phase domains, which acted as scattering centers and reduced the thermal conductivity.

4. Dominant phonon scattering mechanisms in heusler crystal structures

Heusler alloys can be conveniently doped by replacing the elements in the fcc sub-lattices with other atoms to optimize their thermoelectric properties [55]. The optimum doping concentration often moves the peak of the figure-of-merit of these alloys to the moderate temperature ranges [49,120]. In this range of temperature, the impurity scattering is often significant and dominates the phonon transport as schematically shown in Fig. 10.

To demonstrate the underlying physics of the trend observed in Fig. 10, as a case study of a half-Heusler alloy, the thermal conductivity of NiTiSn was calculated and compared with the experimental data (Fig. 11a) [121]. The variation of phonon mean free path (MFP) versus phonon wavelength was also calculated as shown in Fig. 11.b. This plot demonstrates the contributions of various phonon wavelengths and MFP to the thermal conductivity. Model calculations followed the methodology described in Refs. [102,122].

In Fig. 11.b, the green dot-line following by the blue, and red dot-lines represent the contribution of phonons with MFP > 100 nm to the accumulated thermal conductivities (κ_l) at the temperatures of 300 K and 650 K, respectively. Based on this figure, the phonons with MFP > 100 nm contribute to the thermal conductivities equal to 4.8 W/mk at a temperature of 300K. In other word, if all the phonons with MFP > 100 nm are 100% scattered, the thermal conductivities will be reduced by the amount of 4.8 W/mk. However, at a higher temperature of 650K, by eliminating the phonons with the MFP > 100 nm, the thermal conductivity is reduced only by the amount of 2.4 W/mk. Therefore, nanostructuring is much less effective at 650 K (by ~50%) compared to at 300 K. Note that material with grain sizes of 100 nm does not necessarily filter all the phonons with MFP > 100 nm. As discussed earlier, phonons can experience different types of scattering at an interface leading to different kinds of relaxation times such as due to reflection and refraction, diffusive, or Rayleigh scattering. Therefore, the hard cuts as shown in Fig. 11.b are the extreme cases, and in practice, one would need much smaller grains than 100 nm to filter all or most of the phonons with MFP > 100 nm.

Fig. 11.b also shows that the low energy phonons with high MFPs have a small contribution to the overall thermal conductivity, especially at higher temperatures where the half Heusler material has a high zT. In contrast, the accumulated thermal conductivity increases significantly versus phonon energies although the high-energy phonons have smaller MFPs, mainly due to the larger density of states at higher energy.

As mentioned earlier, the scattering of these high-energy (short

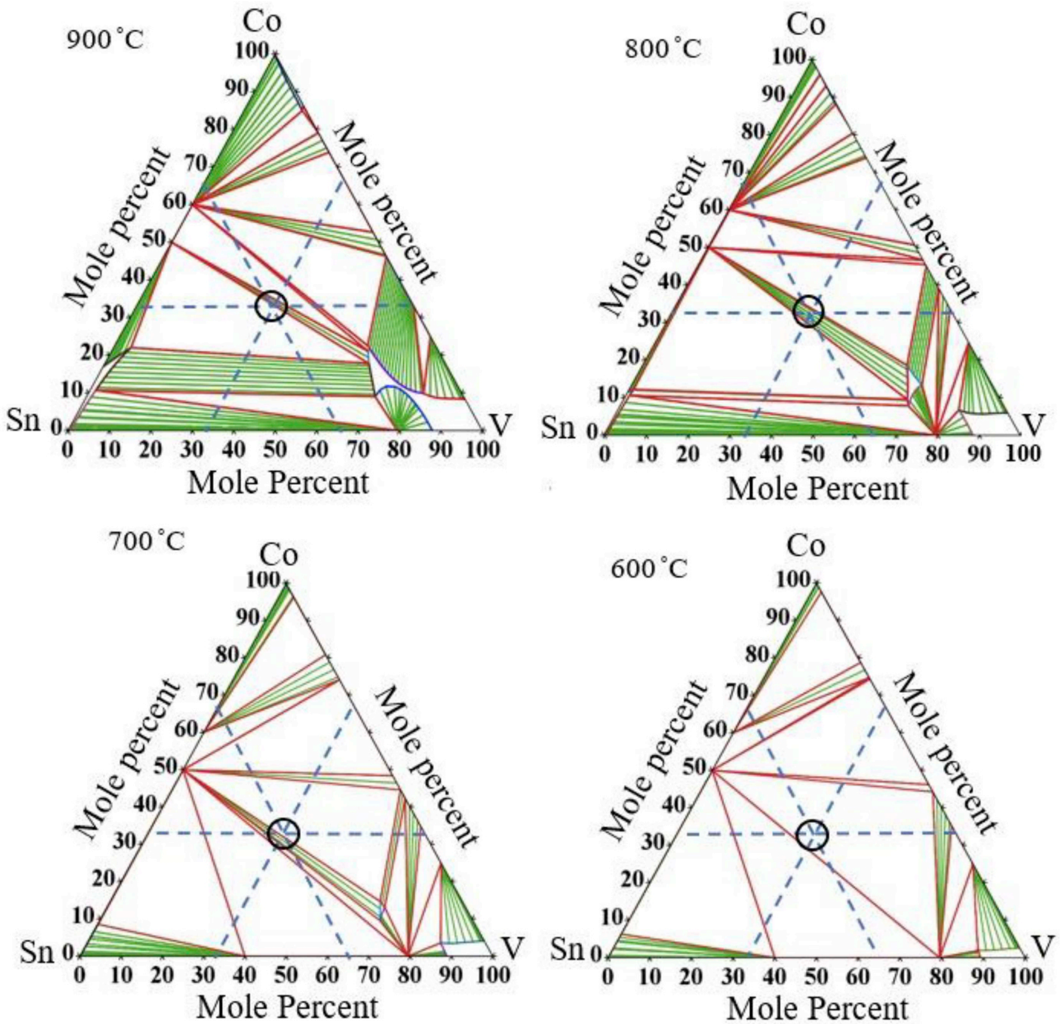

Fig. 9. Multiphase formation by controlling the synthesis temperature of CoVSn.

Table 7
Phase composition of CoVSn alloys at 600,700,800 and 900 °C as mentioned in Fig. 9.

T (°C)	Phase/Crystal structure/Elements
900	Equilibrium line between two areas of (CoSn, BCC (Co,V,Sn)) and (Liquid, CoSn, BCC (Co,V,Sn))
800	Equilibrium line between two areas of (CoSn, BCC (Co,V,Sn)) and (ALTA_Sigma (V, Co), CoSn, BCC (Co,V,Sn))
700	ALTA_Sigma (V, Co) + CoSn + BCC (Co,V,Sn)
600	ALTA_Sigma (V, Co) + CoSn + SnV_3

wavelength) phonons is most efficient through mass and lattice constant fluctuation such as by point defect strategy. Both a_i and M_i in the point defect relaxation time can be manipulated readily by substitutional doping in Heusler compounds to decrease the lattice thermal conductivity effectively.

5. Summary

Thermoelectric generators can contribute to controlling global warming by generating electrical power from low-grade heat which is otherwise wasted in mechanical engines or industrial processes. Heusler semiconductors are known as eco-friendly materials with potentially good thermoelectric properties. The high lattice thermal conductivity of these compounds, however, limited their effectiveness. The transport of

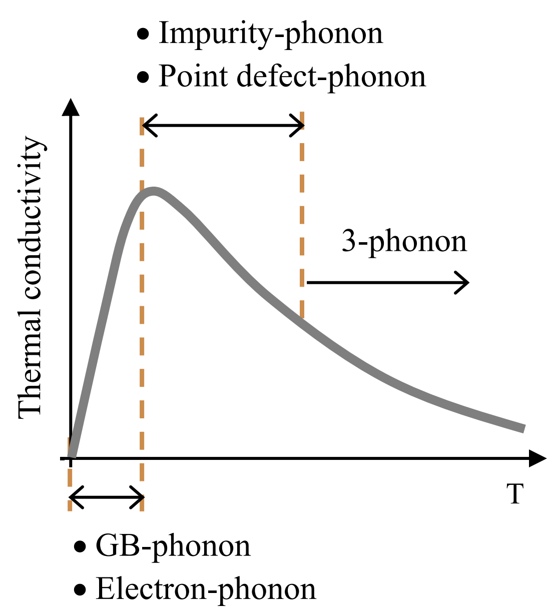

Fig. 10. Dominant phonon scattering mechanisms versus temperature.

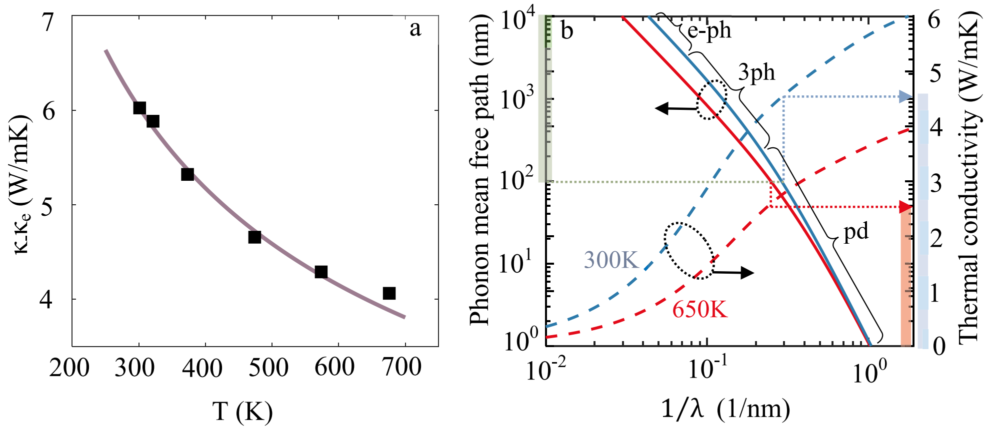

Fig. 11. (a) Thermal conductivity of NiTeSn half-Heusler alloy versus temperature (Symbols: experimental data adapted from Ref. [121] with permission. Line: Theoretical modeling). (b) Comparison of the corresponding phonon mean free path and accumulated thermal conductivity versus reciprocal of phonon wavelength at 300 K and 650 K (e-ph: electron-phonon; 3ph: 3-phonon; pd: point defect).

phonons as the primary heat carriers are to be impaired to reduce thermal conductivity. The critical phonon engineering strategies applicable to Heusler compounds were discussed. These strategies must be implemented according to the working temperature to deliver an effectively low thermal conductivity in practice. At low temperature, the acoustic branches with long wavelength are mainly responsible for heat transfer. These acoustic branches can be distracted by grain/crystal boundaries with length scales comparable to the phonon wavelength. When the grain size is less than the mean free path of these phonons, the thermal conductivity is reduced significantly. By increasing the temperature, the phonons occupy higher frequency states creating mid to short wavelength phonons. In this region, the mass and lattice spacing fluctuations can be more effective in phonon scattering. This can be achieved via substitutional doping of various elements into the Heusler alloy with a large discrepancy of masses and strain fields. The domain interfaces in the multi-phase structures can also generate mass and lattice spacing discontinuities and decrease the thermal conductivity in the medium temperature range. At high temperature, the phonon scattering is often dominated by 3-phonon scattering which is a function of the Grüneisen constant (or the anharmonicity parameter) and is effectively independent of the grain sizes. Among the discussed phonon scattering strategies, the mass and lattice constant fluctuations, due to point defects and/or elemental substitutions, are the most effective methods for improving the thermoelectric performance of Heusler compounds over their optimum working temperature. It should be noted that because of the trade-off between the thermal and the electrical conductivity, the phonon scattering strategies must be implemented carefully as sometimes these methods may cause a significant reduction of the thermoelectric power factor.

Acknowledgment

This work has been supported by the Australian Government Research Training Program Scholarship and The ARC Research Hub for Graphene Enabled Industry Transformation at the University of Adelaide. Also, this study is partially based upon work supported by the National Science Foundation (NSF) under grant numbers ECCS-1351533, ECCS-1711253, and CMMI-1363485.

References

[1] Geoff Martin ES. Effectiveness of state climate and energy policies in reducing power-sector CO2 emissions. Nat Clim Change 2017;7:912–9.
[2] Makeover E. Australia's top 20 greenhouse gas emitters. 2018.
[3] Martin Drechsler JE, Lange Martin, Frank Masurowski, Meyerho Jürgen, Oehlmann Malte. Efficient and equitable spatial allocation of renewable power plants at the country scale. Nat Energy 2017;2:1–9.
[4] Talal Yusaf SG, Borserio JA. Potential of renewable energy alternatives in Australia. Renew Sustain Energy Rev 2011;15:2214–21.
[5] Pragya Nema RKN. Saroj Rangnekar, Minimization of green house gases emission by using hybrid energy system for telephony base station site application. Renew Sustain Energy Rev 2010;14:1635–9.
[6] Zaferani SH. Energy sources, economic policies and sustainable technologies. Environmental science & engineering. Houston, TX 77072: SP LLC Publisher; 2017.
[7] World energy outlook-2017 (WEO-2017). 2017 Available from: http://www.iea.org.
[8] Yadav MK, B.S. First principles study of thermoelectric properties of Li-based half-Heusler alloys. J Alloy Comp 2015;622:388–93.
[9] Ding LC, A.A, Tan L. A review of power generation with thermoelectric system and its alternative with solar ponds. Renew Sustain Energy Rev 2018;81:799–812.
[10] Elsheikh Mohamed Hamid, D.A.S, Sabri Mohd Faizul Mohd, Said Suhana Binti Mohd, Hassan Masjuki Haji, Bashir Mohamed Bashir Ali, Mohamad Mahazani. A review on the moelectric renewable energy : principle parameters that affect their performance. Renew Sustain Energy Rev 2014;30:337–55.
[11] Xi Hongxia, Luo Lingai, Fraisse Gilles. Development and applications of solar-based thermoelectric technologies. Renew Sustain Energy Rev 2007;11:923–36.
[12] Mena JM, H.G.S, Gruhn T, Emmerich H. Ab initio study of domain structures in half-metallic CoTi1-xMnxSb and thermoelectric CoTi1-xScxSb half-Heusler alloys. J Alloy Comp 2015;650:728–40.
[13] Zaferani SH. Using silane products on fabrication of polymer-based nanocomposite for thin film thermoelectric devices. Renew Sustain Energy Rev 2017;71:359–64.
[14] Abdolvand R, Vashaee D. Nanowire thermoelectric infrared detector. WO patent 2013, abdolvand reza. Vashaee Daryoosh USA; Sep. 26, 2013.
[15] D Vashaee AS. HgCdTe superlattices for solid-state cryogenic refrigeration. Appl Phys Lett 2006;88(13). 132110-132110.
[16] Amirkoushyar Ziabari MZ, Vashaee Daryoosh, Ali Shakouri. Nanoscale solid-state cooling: a review. Rep Prog Phys 2016;79.
[17] F Suarez DP, Ladd C, Vashaee D, Dickey MD, Öztürk MC. Flexible thermoelectric generator using bulk legs and liquid metal interconnects for wearable electronics. Appl Energy 2017;202:736–45.
[18] Lobat Tayebi ZZ, Vashaee Daryoosh. Design optimization of microfabricated thermoelectric devices for solar power generation. Renew Energy 2014;66:166–73.
[19] Nozariasbmarz A, A.T.R, Zamanipour Z, Krasinski JS, Tayebi L, Vashaee D. Enhancement of thermoelectric power factor of silicon germanium films grown by electrophoresis deposition. Scripta Mater 2013;69(7):549–52.
[20] Zahra Zamanipour XS, Dehkordi Arash M, Krasinski Jerzy S, Vashaee Daryoosh. The effect of synthesis parameters on transport properties of nanostructured bulk thermoelectric p-type silicon germanium alloy. Phys Status Solidi 2012;209(10):2049–58.
[21] Zamanipour Z, X.S, Mozafari M, Krasinski JS, Tayebi L, Vashaee D. Synthesis, characterization, and thermoelectric properties of nanostructured bulk p-type MnSi1.73, MnSi1.75, and MnSi1.77. Ceram Int 2013;39(3):2353–8.
[22] Sumithra S, T NJ, Misra DK, Nolting WM, Poudeu PFP, Stokes KL. Adv. Energy Mater. 2011;1:1141–7.
[23] Zamanipour Z, V D. J Appl Phys 2012;112.
[24] Zamanipour Zahra, V D. Comparison of thermoelectric properties of p-type nanostructured bulk Si0.8Ge0.2 alloy with Si0.8Ge0.2 composites embedded with CrSi2 nano-inclusions. J Appl Phys 2012;112.
[25] Snyder GJ, T.E.S. Complex thermoelectric materials. Nat Mater 2008;7(2):105–14.
[26] P Norouzzadeh CM, Vashaee D. J Phys Condens Matter 2013;25(47).
[27] P Norouzzadeh CM, Vashaee D. J Appl Phys 2013;114(16).
[28] Norouzzadeh Payam, M CW, Vashaee Daryoosh. Prediction of giant thermoelectric power factor in type-VIII clathrate Si46. Nature 2014(4):7028. Scientific Reports.
[29] Norouzzadeh P, M CW, Vashaee D. Prediction of a large number of electron pockets near the band edges in type-VIII clathrate Si46 and its physical properties from first principles. J Phys: Condens Matter 2013;25.
[30] Heremans JP, V.J, Toberer ES, Saramat A, Kurosaki K, Charoenpakdee A, Yamanaka S, Snyder G. Science 2008;32(554).
[31] Vashaee D, Z Y, Shakouri A, Zeng G, Chiu YJ. Phys Rev B 2006;74(19).
[32] Daryoosh Vashaee JC, Zhang Yan, Ali Shakouri, Zeng Gehong, LaBounty Chris, Fan Xiaofeng, Piprek Joachim, Bowers John E, Croke Edward. MODELING AND OPTIMIZATION OF SINGLE-ELEMENT BULK SiGe THIN-FILM COOLERS. Microscale Thermophys Eng 2004;8(2):99–118.

[33] Zide JMO, V D, Bian ZX, Zeng G, Bowers JE, Shakouri A, Gossard AC. Phys Rev B Condens Matter 2006;74.
[34] Vashaee D, S A. Phys Rev Lett 2004;92(10).
[35] Vashaee D, S A. J Appl Phys 2004;95(3).
[36] Vashaee D, S A. J Appl Phys 2007;101(5):1–5.
[37] Payam Norouzzadeh KFE, Vashaee Daryoosh. The effect of nanostructuring on the spectral population of electrons and phonons. J Alloy Comp 2018;753:234–8.
[38] Milad Mohebali YL, Tayebi Lobat, Krasinski Jerzy S, Vashaee Daryoosh. Thermoelectric figure of merit of bulk FeSi2-Si0.8Ge0.2 nanocomposite and a comparison with β-FeSi2. Renew Energy 2015;74:940–7.
[39] Amin Nozariasbmarz ZZ, Norouzzadeh Payam, Krasinski Jerzy S, Vashaee Daryoosh. Enhanced thermoelectric performance in a metal/semiconductor nanocomposite of iron silicide/silicon germanium. RSC Adv 2016;6:49643–50.
[40] Keppens V, M D, Sales B, Chakoumakos B, Dai P, Coldea R, Maple M, Gajewski D, Freeman E, Bennington S. Nature 1998;395(876). (London).
[41] Hermann RP, J R, Schweika W, Grandjean F, Mandrus D, Sales BC, Long GJ. Phys Rev Lett 2003;90.
[42] Koza MM, J MR, Viennois R, Mutka H, Girard L, Ravot D. Nat Mater 2007;7(805).
[43] Norouzzadeh Payam, C.W.M. Daryoosh Vashaee, Phonon dynamics in type VIII Si clathrates: beyond the rattler concept. Phys Rev B 2017;95.
[44] Norouzzadeh P, C.W.M, Vashaee D. Electronic, elastic, vibrational, and thermodynamic properties of type-VIII clathrates Ba8Ga16Sn30 and Ba8Al16Sn30 by first principles. J Appl Phys 2013;114.
[45] Norouzzadeh P, C.W.M, Vashaee D. Structural, electronic, phonon and thermodynamic properties of hypothetical type-VIII clathrates Ba8Si46 and Ba8Al16Si30 from first principles. J Alloy Comp 2013;587:474–80.
[46] Ahmed R, N.S.M, Ul Haq B, Shaari A, Alfaifi S, Butt FK, Muhamad MN, Ahmed M, Tahir SA. Investigations of electronic and thermoelectric properties of half-Heusler alloys XMgN (X = Li, Na, K) by first-principles calculations. Mater Des 2017;136:196–203.
[47] Visconti A, N C, Leforestier J, Mingo N, Bernard-Granger G. Influence of the addition of HfO2 particles on the thermoelectric properties of an N-type half-Heusler alloy sintered by spark plasma sintering. J Alloy Comp 2017;709:36–41.
[48] Poon GJ. Chapter 2 Electronic and thermoelectric properties of Half-Heusler alloys. Semiconductors and semimetals. Elsevier; 2001. p. 37–75.
[49] Wenjie Xie AW, Tang Xinfeng, Zhang Qingjie, Poon Joseph, Tritt Terry M. Recent advances in nanostructured thermoelectric half-heusler compounds. Nanomaterials 2012;2:379–412.
[50] Zeier Wolfgang G, J.S, Hautier Geoffroy, Aydemir Umut, Gibbs Zachary M, Felser Claudia, Jeffrey Snyder G. Engineering half-Heusler thermoelectric materials using Zintl chemistry. Nat Rev Mater 2016;1:1–10.
[51] Stefano Sanvito CO, Xue Junkai, Tiwari Anurag, Zic Mario, Archer Thomas, Tozman Pelin, Venkatesan Munuswamy, Coey Michael, Curtarolo Stefano. Accelerated discovery of new magnets in the Heusler alloy family. Sci Adv 2017;3:1–9.
[52] Ahamed R, G R, Xie Z, Chen L, Munroe P, Xu S. Powder processing and characterisation of a quinary Ni-Mn-Co-Sn-Cu Heusler alloy. Powder Technol 2018;324:69–75.
[53] Ferromagnetic shape memory heusler materials: synthesis, microstructure characterization and magnetostructural properties. Materials 2018;11(988):1–34.
[54] Mohankumar R, S.R, Rajagopalan M, Manivel Raja M, Kamat SV, Kumar J. Effect of Fe substitution on the electronic structure, magnetic and thermoelectric properties of Co2FeSi full Heusler alloy: a first principle study. Comput Mater Sci 2015;109:34–40.
[55] Tanja Graf CF, Parkin Stuart SP. Simple rules for the understanding of Heusler compounds. Prog Solid State Chem 2011;39:1–50.
[56] Galanakis I. Theory of heusler and full-heusler compounds. In: Felser AHC, editor. Heusler alloys. Springer; 2016.
[57] Gunn C. Periodic table Available from: http://www.science-teachers.com/printable_periodic_tables.htm.
[58] Katsuyama S, R.M, Ito M. Thermoelectric properties of half-Heusler alloys Zr1 − xYxNiSn1 − ySby. J Alloy Comp 2007;428:262–7.
[59] Kaller M, D.F, Gelbstein Y. Sc solubility in p-type half-Heusler (Ti1-cScc)NiSn thermoelectric alloys. J Alloy Comp 2017;729:446–52.
[60] Misra PK. Phonons and lattice vibrations. Physics of condened matter. US: Elsevier; 2011. p. 688.
[61] Kim W. Strategies for engineering phonon transport in thermoelectrics. J Mater Chem C 2015;3:10336–48.
[62] Prashun Gorai VS, Toberer Eric S. Computationally guided discovery of thermoelectric materials. Nat Rev Mater 2017;2:1–16.
[63] Balandin AA. Thermal properties of graphene and nanostructured carbon materials. Nat Mater 2011;10:569–81.
[64] Matthias Schrade KB, Eliassen Simen NH, Guzik Matylda N, Echevarria-Bonet Cristina, Sørby Magnus H, Jenuš Petra, Hauback Bjørn C, Tofan Raluca, Gunnæs Anette E, Persson Clas, Løvvik Ole M, Finstad Terje G. The role of grain boundary scattering in reducing the thermal conductivity of polycrystalline XNiSn (X = Hf, Zr, Ti) half-Heusler alloys. Sci Rep Nat 2017;7:1–7.
[65] Yaw Wang Chai TO, Kenjo Takahiro, Kimura Yoshisato. The effect of an isoelectronic TieZr substitution on Heusler nanoprecipitation and the thermoelectric properties of a (Ti0.2,Zr0.8) Ni1.1Sn half-Heusler alloy. J Alloy Comp 2016;662:566–77.
[66] Jiong Yang LX, Qiu Wujie, Wu Lihua, Shi Xun, Chen Lidong, Yang Jihui, Zhang Wenqing, Uher Ctirad, Singh David J. On the tuning of electrical and thermal transport in thermoelectrics: an integrated theory–experiment perspective. npj Comput Mater Nat 2016;2:1–17.
[67] Kittel C. Introduction to solid state physics. New York: John Wiley & Sons; 2004.
[68] Holland MG. Analysis of lattice thermal conductivity*. Phys Rev 1963;132(6):2461–71.
[69] Ramachandran B, Y.H.L, Kuo YK, Kuo CN, Gippius AA, Lue CS. Thermoelectric properties of Heusler-type Ru2VAl1 − xGax alloys. Intermetallics 2018;92:36–41.
[70] Steigmeier EF,AB. Phys Rev 1964;136(A1149).
[71] Callaway J. Model for lattice thermal conductivity at low temperatures. Phys Rev 1959;113(1046).
[72] Nikhil Satyala PN. Daryoosh vashaee, nano bulk thermoelectrics: concepts, techniques, and modeling. Thermoelectrics at nanoscale. Springer; 2014. p. 141–83.
[73] Nikhil Satyala DV. Modeling of thermoelectric properties of magnesium silicide (Mg2Si). J Electron Mater 2012;41(6):1785–91.
[74] Ziman JM. Philos Mag 1957;2(192).
[75] Ziman RM. Philos Mag 1956;1(191).
[76] Pomeranchuk I. On the thermal conductivity of dielectrics. Phys Rev 1941:60.
[77] Pomeranchuk I. On the thermal conductivity of dielectrics at temperatures lower than that of debye. J Phys 1942;6(6):235–50.
[78] Ferry DK. Semiconductor transport. London: Taylor & Francis; 2000.
[79] Lee P, S.C.T, Chao L. High-temperature thermoelectric properties of Tix(ZrHf)0.99 − xV0.01Ni0.9Pd0.1Sn0.99Sb0.01 half-Heusler alloys. J Alloy Comp 2010;496:620–3.
[80] Lee P, L.C. High-temperature thermoelectric properties of Ti0.5(ZrHf)0.5 − xNbxNi0.9Pd0.1Sn0.98Sb0.02 half-Heusler alloys. J Alloy Comp 2010;504:192–6.
[81] de Boor J, S.G, Kolb H, Dasgupta T, Mueller E. Thermoelectric transport and microstructure of optimized Mg2Si0.8Sn0.2. J Mater Chem C 2015;3:10467–75.
[82] Maji P, J.P.A.M, Zhou X, Chi H, Uher C, Poudeu PFP. Thermoelectric performance of nanostructured p-type Zr0.5Hf0.5Co0.4Rh0.6Sb1 − xSnx half-Heusler alloys. J Solid State Chem 2013;202:70–6.
[83] Michael Schwall BB. On the phase separation in n-type thermoelectric half-heusler materials. Materials 2018;649(11).
[84] Pramathesh Maji NT, Misra DineshK, HeikeGabrisch Kevin Stokes, Poudeu PierreFP. Effects ofRhonthethermoelectricperformanceofthe p-type Zr0.5Hf0.5Co1 xRhxSb0.99Sn0.01 half-Heusler alloys. J Solid State Chem 2010;183:1120–6.
[85] Appel O, T.Z, Kalabukhov S, Beeri O, Gelbstein Y. Morphological effects on the thermoelectric properties of Ti0.3Zr0.35Hf0.35Ni1 + dSn alloys following phase separation. J Mater Chem C 2015;3:11653–9.
[86] Bouyrie Y, C.C, Ohorodniichuk V, Malaman B, Dauscher A, Tobola J, Lenoir B. Crystal structure, electronic band structure and high-temperature thermoelectric properties of Te-substituted tetrahedrites Cu12Sb4-xTexS13 (0.5 ≤ x ≤ 2.0). J Mater Chem C 2015;3:10476–87.
[87] Biswas SNGaK. Sb deficiencies control hole transport and boost the thermoelectric performance of p-type AgSbSe2. J Mater Chem C 2015;3:10415–21.
[88] Hu Y, S.K.B, Grebenkemper JH, Kauzlarich SM. The effect of light rare earth element substitution in Yb14MnSb11 on thermoelectric properties. J Mater Chem C 2015;3:10566–73.
[89] Liu Z, G H, Shuai J, Wang Z, Mao J, Jie Q, Wang D, Cai W, Sui J, Ren Z. The effect of Nickel doping on electron and phonon transport in n-type nanostructured thermoelectric material CoSbS. J Mater Chem C 2015;3:10442–50.
[90] Ma JM, S.M.C, Zeier WG, Vo T, Allmen PV, Snyder GJ, Kaner RB, Fleurial J, Bux SK. Mechanochemical synthesis and high temperature thermoelectric properties of calcium-doped lanthanum telluride La 3 - x Ca x Te 4. J Mater Chem C 2015;3:10459–66.
[91] Pan Y, T.W, Wu C, Li J. Electrical and thermal transport properties of spark plasma sintered n-type Bi2Te3-xSex alloys: the combined effect of point defect and Se content. J Mater Chem C 2015;3:10583–9.
[92] Rausch E, B.B, Stahlhofen JM, Ouardi S, Burkhardt U, Felser C. Fine tuning of thermoelectric performance in phase-separated half-Heusler compounds. J Mater Chem C 2015;3:10409–14.
[93] Visconti A, G GB, Navone C, Leforestier J, Mingo N. Microstructure investigations and thermoelectric properties of an N-type Half-Heusler alloy sintered by spark plasma sintering. Scripta Mater 2016;123:100–4.
[94] Chen G. Nanoscale energy transport and conversion. New York: Oxford University Press; 2005.
[95] Mikami M, K.K. Effect of Bi addition on microstructure and thermoelectric properties of Heusler Fe2VAl-sintered alloy. J Alloy Comp 2008;466:530–4.
[96] Shigeru Katsuyama TK. Effect of mechanical milling on thermoelectric properties of half-Heusler ZrNiSn0.98Sb0.02 intermetallic compound. Mater Sci Eng, B 2010;166(1):99–103.
[97] Sin-Shien Lin C-NL. Effect of ball milling and post treatment on crystal defects and transport properties of Bi2(Se,Te)3 compounds. J Appl Phys 2011;110:1–7.
[98] Meng-Pei Lu C-NL. Mechanical and thermal processing effects on crystal defects and thermoelectric transport properties of Bi2(Se,Te)3 compounds. J Alloy Comp 2013;571:178–82.
[99] Yecheng Zhou WL, Wu Minghui, Zhao Li-Dong, He Jiaqing, Wei Su-Huai, Huang Li. Influence of defects on the thermoelectricity in SnSe: a comprehensive theoretical study. Phys Rev 2018;97:1–8.
[100] Son JH, M.W.O.B.S.K.S.D.P, Min BK, Kim MH, Lee HW. Effect of ball milling time on the thermoelectric properties of p-type (Bi,Sb)2Te3. J Alloys Comp 2013;566:168–74.
[101] Bhattachary S, M.J.S, Russell M, Tritt TM, Xia Y, Ponnambalam V, Poon SJ, Thadhani N. Effect of boundary scattering on the thermal conductivity of TiNiSn-based half-Heusler alloys. Phys Rev B 2008;77(18).
[102] Nikhil Satyala DV. The effect of crystallite size on thermoelectric properties of bulk nanostructured magnesium silicide (Mg2Si) compounds. Appl Phys Lett 2012;100(7).
[103] Payam Norouzzadeh ZZ, Krasinski Jerzy S, Vashaee Daryoosh. The effect of nanostructuring on thermoelectric transport properties of p-type higher manganese

silicide MnSi1.73. J Appl Phys 2012;112(12):1–7.
[104] Mohamed S, El-Asfoury MNAN, Nakamura Koichi, Abdel-Moneim Ahmed. Enhanced thermoelectric performance of Bi85Sb15-graphene composite by modulation carrier transport and density of state effective mass. J Alloy Comp 2018;745:331–40.
[105] Khushboo Agarwal VK, Varandani Deepak, Dhar Ajay, Mehta BR. Nanoscale thermoelectric properties of Bi2Te3 e Graphene nanocomposites: conducting atomic force, scanning thermal and kelvin probe microscopy studies. J Alloy Comp 2016;681:394–401.
[106] Shupin Zhang AL, Sun Kangning. Thermoelectric properties of Graphene/ Mn0.7Zn0.3Fe2O4 composites. Ceram Int 2017;43:8643–7.
[107] Haijie Chen CY, Liu Huili, Zhang Ganghua, Wan Dongyun, Huang Fuqiang. Thermoelectric properties of CuInTe2/graphene composites. CrystEngComm 2013;15:6648–51.
[108] Chenguang Fu HX, Zhu TJ, Xie Jian, Zhao XB. Enhanced phonon scattering by mass and strain field fluctuations in Nb substituted FeVSb half-Heusler thermoelectric materials. J Appl Phys 2012;112(12).
[109] Ben Huang PZ, Xuqiu Yang, Guodong LI. Effects of mass fluctuation on thermal transport properties in bulk Bi2Te3. J Electron Mater 2016;46(5):2797–806.
[110] Tanya Berry CF, Auffermann Gudrun, Fecher Gerhard H, Walter Schnelle, Serrano-Sanchez Federico, Yuan Yue, Liang Hong. Claudia felser, enhancing thermoelectric performance of TiNiSn half-heusler compounds via modulation doping. Chem Mater 2017;29:7042–8.
[111] Mohamed S, El-Asfoury MNAN, Nakamura Koichi, Abdel-Moneim Ahmed. Thermoelectric power factor performance of Bi85Sb15/graphene composite. Jpn J Appl Phys 2016;55:1–5.
[112] Mikami M, S.T, Kobayashi K. Thermoelectric properties of Sb-doped Heusler Fe2VAl alloy. J Alloy Comp 2009;484:444–8.
[113] Chai YW, K.Y, Kimura Y. Intrinsic point defects in thermoelectric half-Heusler alloys. Scripta Mater 2014;83:13–6.
[114] Michael Schwallab BB. Phase separation as a key to a thermoelectric high efficiency. Phys Chem Chem Phys 2013;15:1868–72.
[115] Soven P. Coherent-potential model of substitutional disordered alloys. Phys Rev 1967;809(156).
[116] Sheng P. Introduction to wave scattering, localization and mesoscopic phenomena. Berlin Heidelberg: Springer-Verlag; 2006.
[117] Economou EN. Green's function in quantum physics. New York: Springer-Verlag; 1979.
[118] Jason E, Douglas, B CS, Miao Mao-Sheng, Torbet Chris J, Stucky Galen D, Pollock Tresa M, Seshadri Ram. Enhanced thermoelectric properties of bulk TiNiSn via formation of a TiNi2Sn second phase. Appl Phys Lett 2012;101(18).
[119] Yuewen Zhang HM, Bing Sun a, Liu Binwu, Liu Haiqiang, Kong Lingjiao, Liu Baomin, Jia Xiaopeng, Chen Xin. Thermoelectric performance of graphene composited BiSbTe bulks by high pressure synthesis. J Alloy Comp 2017;715:344–8.
[120] Shuo Chen ZR. Recent progress of half-Heusler for moderate temperature thermoelectric applications. Mater Today 2013;16(10):387–95.
[121] Hiroaki Muta TK, Kurosaki Ken, Yamanaka Shinsuke. High-temperature thermoelectric properties of Nb-doped MNiSn (M = Ti, Zr) half-Heusler compound. J Alloy Comp 2009;469:50–5.
[122] Minnich AJ, L H, Wang XW, Joshi G, Dresselhaus MS, Ren ZF, Chen G, Vashaee D. Modeling study of thermoelectric SiGe nanocomposites. Phys Rev B 2009:80.